Supporting Information

Inhibition of Vanadium Cathode Dissolution in Zinc Ion batteries Via Niobium Pillaring

Shenglong Wu, [a] Yang Zhang, [a] Yue Zhu, [a] Wenzhen Du, [a] Jie Wu, [a] Weijie Zhang, [a] Qiongguang Li [a,b,c*]

[a] Anhui Province International Research Center on Advanced Building Materials, School of Materials and Chemical Engi-neering, Anhui Jianzhu University, Hefei 230601, China

[b] Key Laboratory of Functional Molecular Solids, Ministry of Education, Anhui Normal University, Wuhu 230061, China

[c] Anhui Institute of Strategic Study on Carbon Dioxide Emissions Peak and Carbon Neutrality in Urban-Rural Development, Anhui Jianzhu University, Hefei 230601, China

[*]Corresponding authors.

E-mail addresses: qgli@ahjzu.edu.cn (Qiongguang Li)

Experimental Section

Chemicals

V_2O_5, PEG-4000, $NbCl_5$ and H_2O_2 with analytical purity were purchased from Shanghai Macklin Biochemical Technology Co., Ltd. All chemicals were used without further treatment.

Material Preparation

5 mmol of V_2O_5 and x mmol of $NbCl_5$, add 60 ml of deionized water, and stir for 10 minutes. add 12 ml of H_2O_2, continue stirring until the solution turns from yellow to burgundy, then add 0.03 g of PEG-4000, stir again for 80 minutes, transfer the burgundy solution to a 100 ml Teflon-lined high-pressure reactor, and heat treat at 200°C for 36 hours. Centrifuge to collect the green product, and wash several times with water and ethanol. Finally, dry the washed product overnight at 50°C. The products with x= 0.05, 0.067 and 0.1 are denoted as PNVO-1, PNVO-2 and PNVO-3, respectively. By contrast, PVO was prepared using the same procedure but without the addition of $NbCl_5$. VO was prepared using the same procedure but without the addition of PEG-4000 and $NbCl_5$.

Materials characterization

Scanning electron microscope and transmission electron microscope images were collected from ZEISS Sigma 300 (Germany) and FEI Talos F200x (the United States), respectively. Electron paramagnetic resonance and X-ray photoelectron spectroscopy measurements were carried out on Bruker EMXplus-6/1 (Germany) and Thermo Scientific K-Alpha (the United States), respectively. Powder X-ray diffraction patterns were measured on Rigaku SmartLab with Cu-Kα radiation. Raman signals were

recorded on Renishaw inVia reflex confocal microscopy Raman spectrometer (England) with an excitation wavelength of 532 nm. Thermogravimetric analysis (TGA) was carried out on an EXSTAR TG/DTA 6300 (Seiko Instruments, Japan) using a heating rate of 10 ℃ min^{-1} under N_2 atmosphere.

Electrochemical test

The working electrode was prepared by coating a Ti foil with a slurry of active materials (70 wt%), super P (20 wt%), and polyvinylidene fluoride (10 wt%), and N-methyl pyrrolidone was employed as solution. And then it was dried at 80 °C in a vacuum oven for 12 h. Electrochemical performances were tested by assembling CR2025 coin-type cells. Zinc foil was used as the counter electrode, and 2M ZnSO4 aqueous solution was used as electrolyte. Glass fiber GF/D was applied as the separator. The galvanostatic charge-discharge experiments were tested on a NEWARE-BTS-4008T-5 V/ 10 mA testing system (Neware Co., Ltd., Shenzhen, China) in a voltage range between 0.2 and 1.6 V. Cyclic voltammetry and electrochemical impedance spectroscopy measurements were carried on a CHI660E electrochemical workstation (Shanghai Chenhua Device Company, China). Galvanostatic intermittent titration technique (GITT) was performed at 1A g^{-1} for 1 min then relaxing for 30 min.

Supplementary Figures

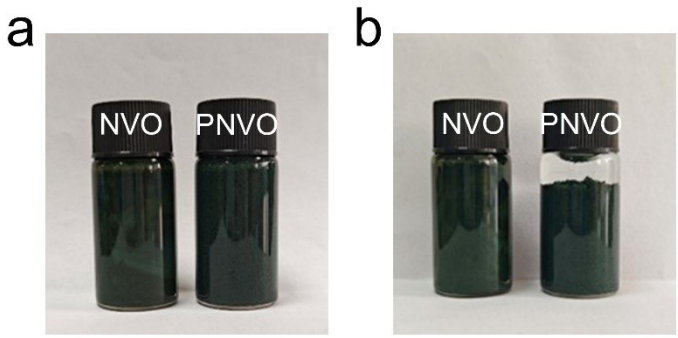

Figure S1. Comparison of NVO and PNVO materials at rest. (a) 0 DAY. (b) 3DAY.

The hydrothermally synthesized NVO and PNVO samples were each poured into separate transparent glass bottles and allowed to stand for three days. After three days, the NVO sample showed no significant change, and even centrifugation could not separate it from the slurry. In contrast, the PNVO sample (prepared with PEG assistance) demonstrated excellent natural sedimentation ability.

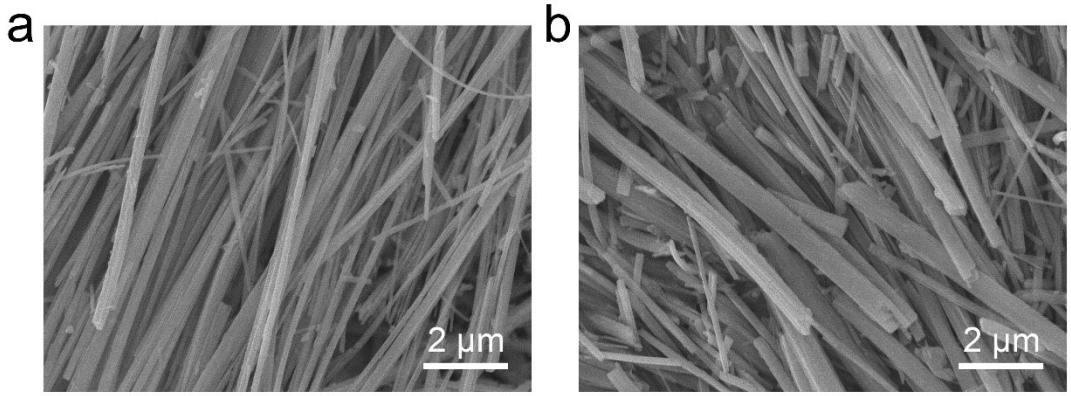

Figure S2. SEM images of (a) PNVO-1 and (b) PNVO-3.

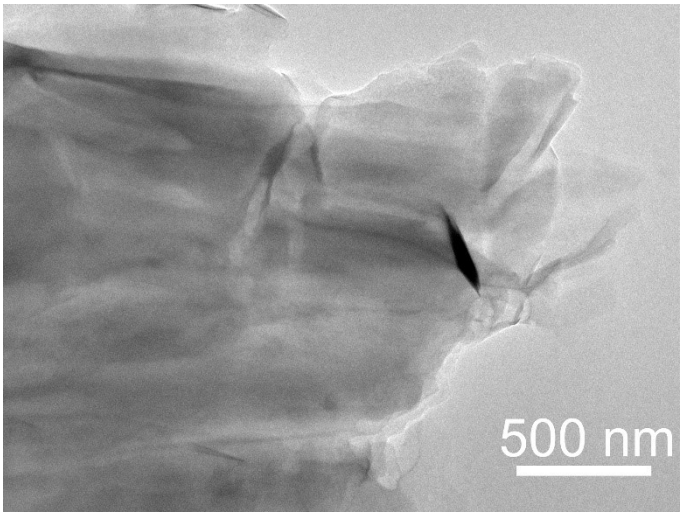

Figure S3. TEM images of VO.

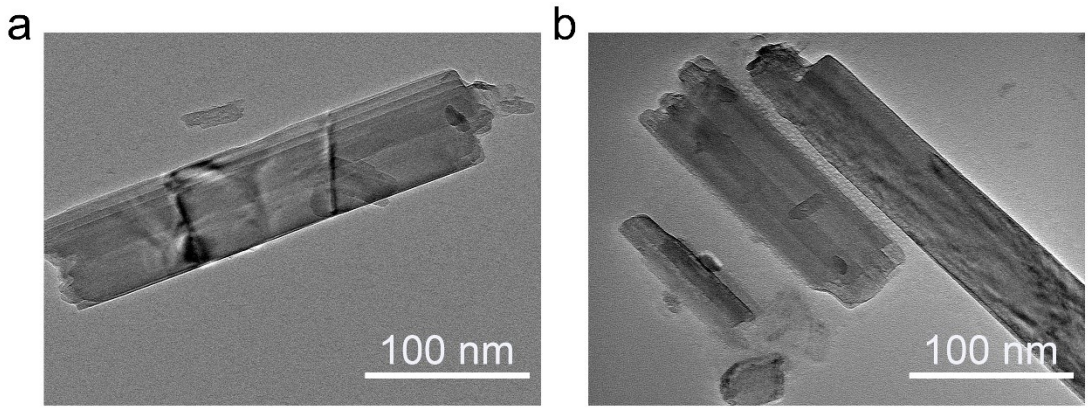

Figure S4. TEM images of (a) PNVO-1 and (b) PNVO-3.

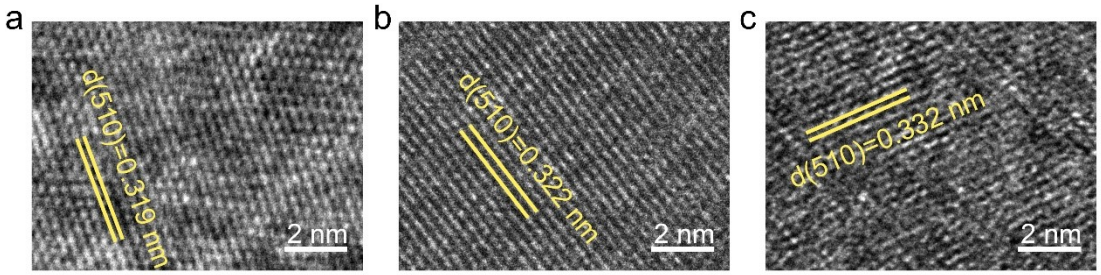

Figure S5. HRTEM images of (a) PVO, (b) PNVO-1 and (c) PNVO-3.

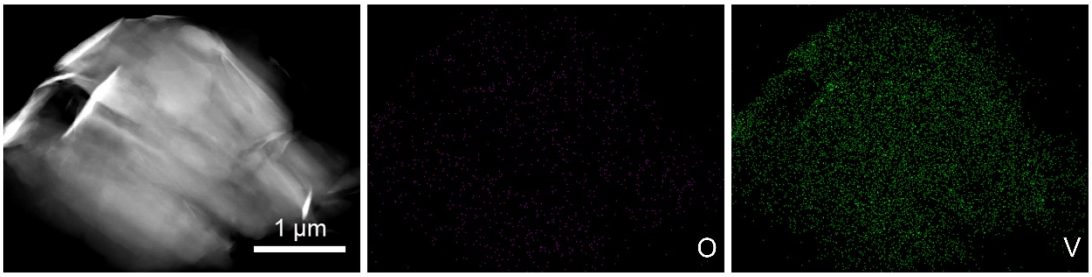

Figure S6. TEM and element mapping images of VO.

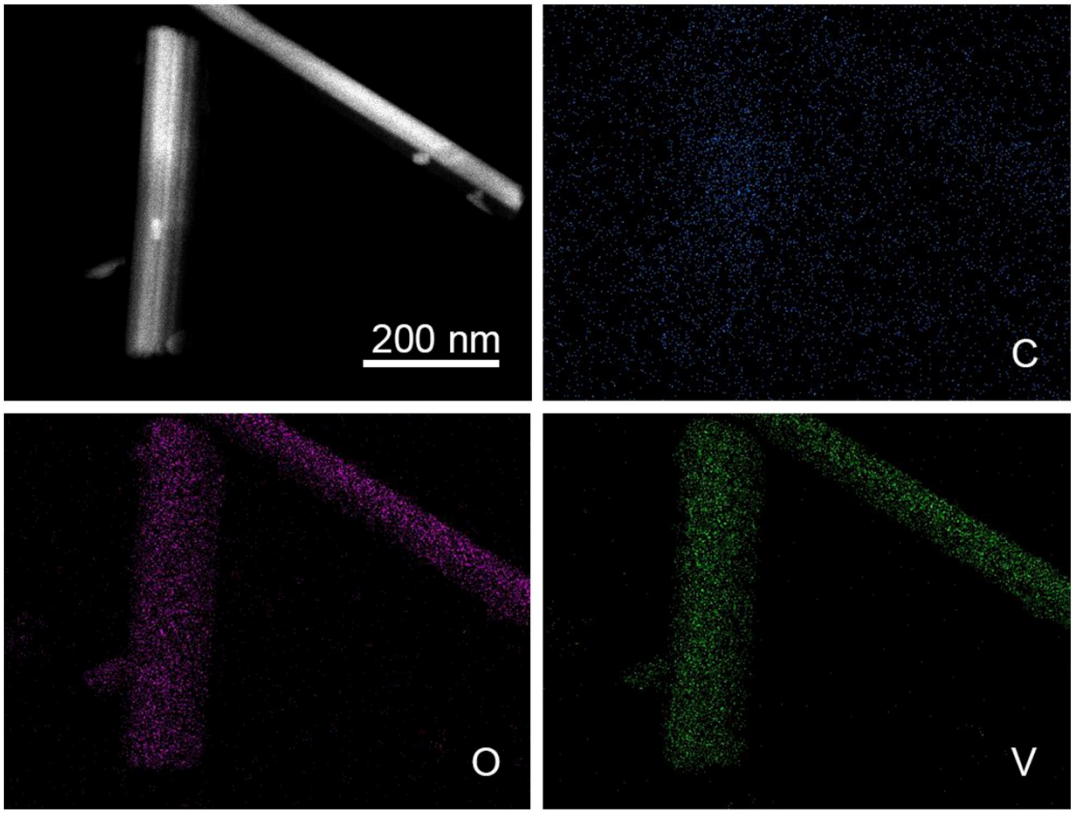

Figure S7. TEM and element mapping images of PVO.

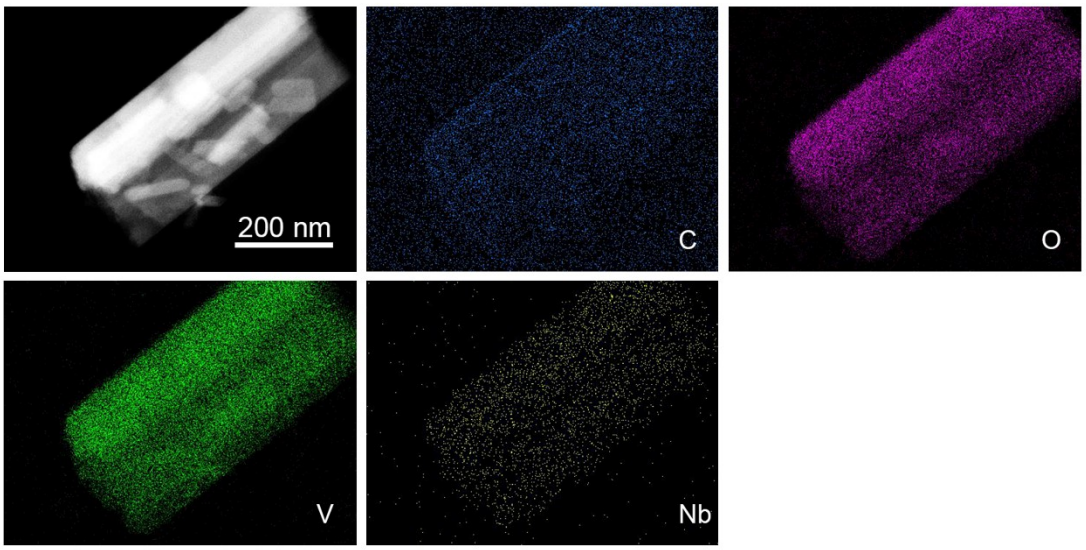

Figure S8. TEM and element mapping images of PNVO-1.

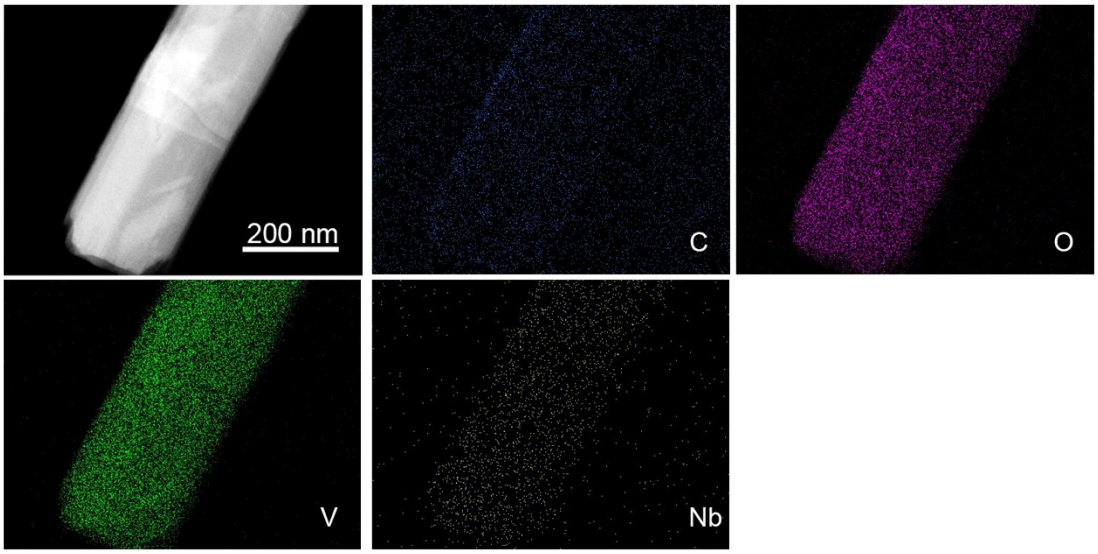

Figure S9. TEM and element mapping images of PNVO-3.

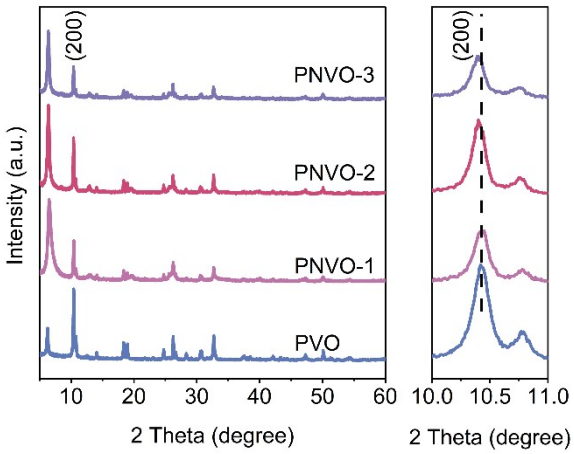

Figure S10. XRD patterns of PVO, PNVO-1, PNVO-2, PNVO-3.

Compared to PVO, the diffraction peak of the (200) crystal plane of PNVO gradually shifts to lower angles with increasing Nb doping concentration, which is related to the spacing expansion caused by the intercalation effect of Nb^{5+}, indicating a gradual increase in the interlayer spacing.[1]

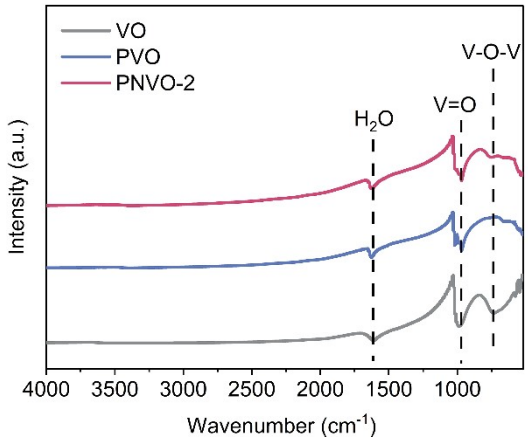

Figure S11. FTIR spectrum of VO, PVO and PNVO-2.

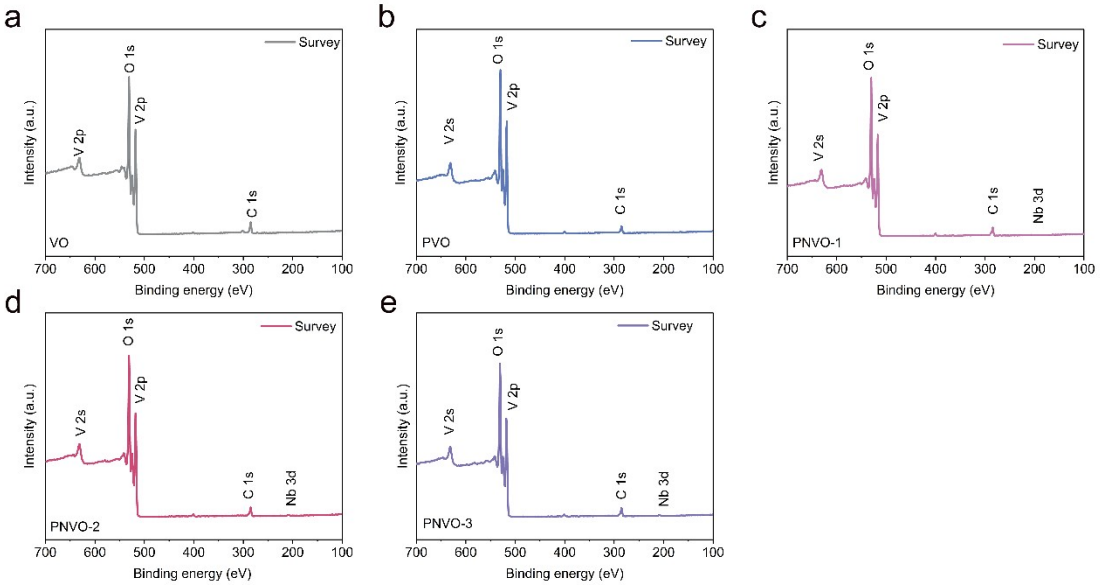

Figure S12. XPS spectra of (a) VO, (b) PVO, (c) PNVO-1, (d) PNVO-2 and (e) PNVO-3.

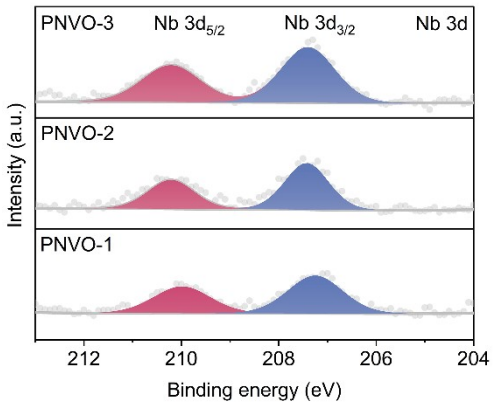

Figure S13. XPS Nb 3d spectra of PNVO-1, PNVO-2 and PNVO-3.

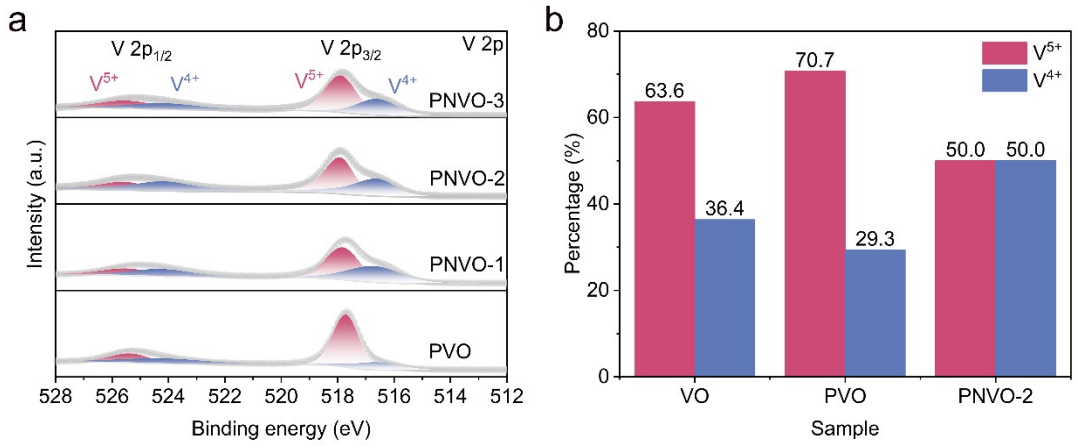

Figure S14. (a) V 2p XPS spectra (b) Fitting results of V^{5+}/V^{4+} ratio for VO, PVO and PNVO-2.

In the V 2p XPS spectra, with increasing Nb doping content, the peak corresponding to V^{4+} in PNVO becomes progressively more prominent. Meanwhile, as shown in Figure S14b, through peak integration of V^{5+} and V^{4+}, the V^{4+} content in PNVO-2 reaches 50%, which is significantly higher than the 36.4% and 29.3% in VO and PVO, respectively. The mixed valence state enhances the electrochemical activity of $V_3O_7 \cdot H_2O$, thereby delivering high reversible capacity.[2]

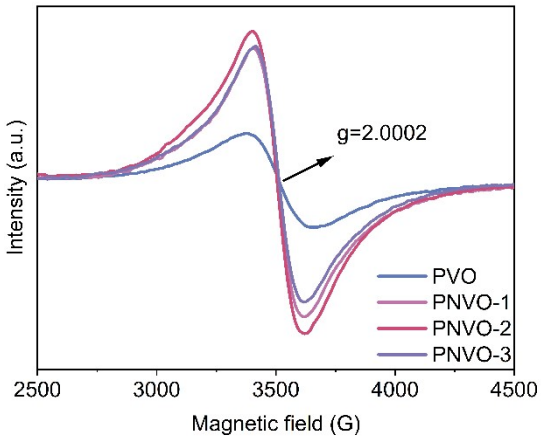

Figure S15. EPR spectra of PVO, PNVO-1, PNVO-2, PNVO-3.

The oxygen vacancy concentration in PNVO is significantly higher than that in PVO, confirming that Nb^{5+} doping successfully introduces abundant oxygen vacancies. Among all samples, PNVO-2 exhibits the strongest EPR signal, indicating the highest oxygen vacancy concentration. This provides abundant electrochemical active sites for PNVO-2, thereby endowing it with excellent rate capability.

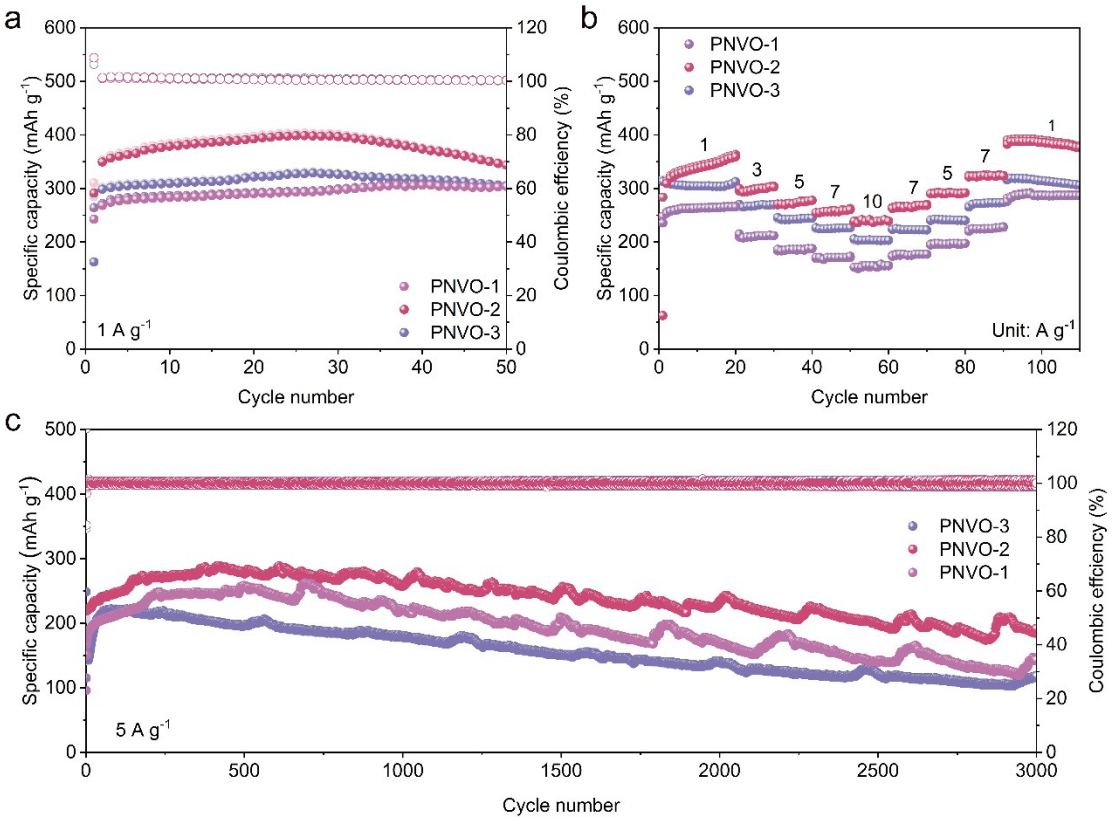

Figure S16. Cycle performance of PNVO-1, PNVO-2 and PNVO-3 at (a) 1 A g^{-1} and (c) 5 A g^{-1}. (b)Rate performance of PNVO-1, PNVO-2 and PNVO-3.

As illustrated in Figure S16a, the capacity of PNVO-2 initially increased before slightly decreasing, achieving a maximum reversible capacity of 403.34mAh g^{-1} at 1 A g^{-1}. The maximum reversible capacity of PNVO-2 was markedly higher than that of PNVO^{-1} and PNVO-3. Furthermore, similar phenomena were observed in cycle performance at 5Ag^{-1}. This is attributed to the activation process. Figure S16b displays the rate performance of PNVO-1, PNVO-2 and PNVO-3. At 1 A g^{-1}, The reversible capacity of PNVO-2 was gradually increased, achieving 381 mAh g^{-1} after 20 cycles. While PNVO-1 and PNVO-3 were 304 mAh g^{-1} and 263 mAh g^{-1} respectively. With the increase of current density, PNVO-2 delivered reversible capacity of 310 mAh g^{-1}, 285 mAh g^{-1}, 266 mAh g^{-1}, 244 mAh g^{-1} at 3 A g^{-1}, 5 A g^{-1}, 7 A g^{-1} and 10 A g^{-1}, superior to 299 mAh g^{-1}, 275 mAh g^{-1}, 259 mAh g^{-1}, 236 mAh g^{-1} for PNVO-1 and 209 mAh

g^{-1}, 186 mAh g^{-1}, 171 mAh g^{-1}, 153 mAh g^{-1} for PNVO-3. During the following cycles, PNVO-2 delivered high reversible capacities of 276 mAh g^{-1}, 303 mAh g^{-1}, 347 mAh g^{-1}, 402 mAh g^{-1} at 7 A g^{-1}, 5 A g^{-1}, 3 A g^{-1} and 1 A g^{-1}, respectively, while the capacities of PNVO-1 and PNVO-3 were 264/177 mAh g^{-1}, 292/196 mAh g^{-1}, 323/224 mAh g^{-1}, 386/287 mAh g^{-1}, respectively. Consequently, PNVO-2 can be reasonably selected as the material with the optimal Nb doping ratio.

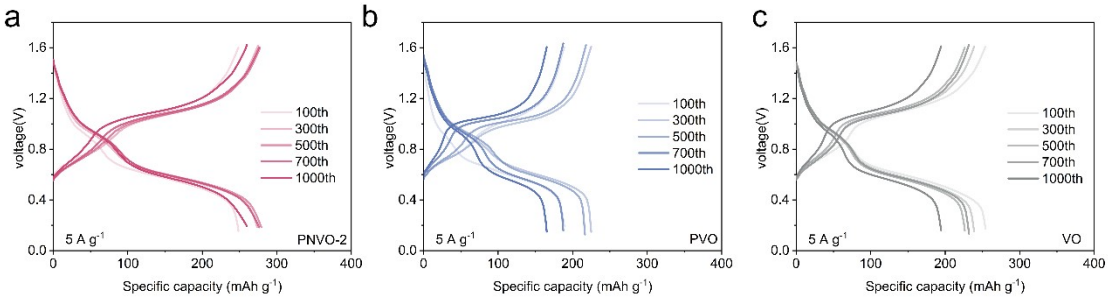

Figure S17. GCD curves of (a) PNVO-2, (b) PNVO-2 and (c) PVO at 5A g^{-1}.

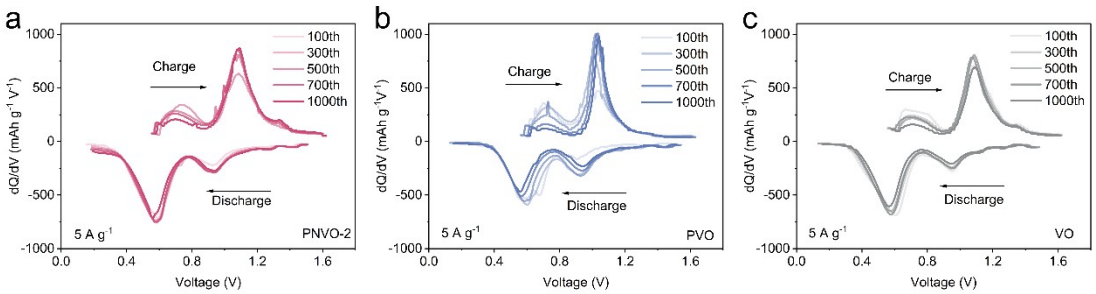

Figure S18. dQ/dV curves of (a) PNVO-2, (b) PVO and (c) VO at various cycle numbers under a current density of 5 A g^{-1}.

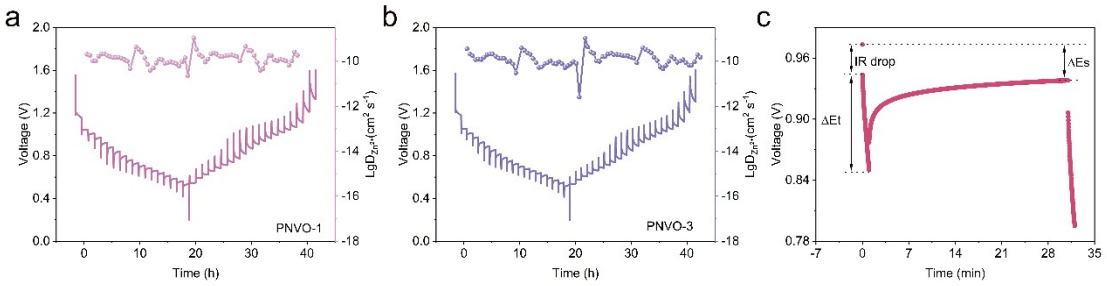

Figure S19. Galvanostatic intermittent titration technique (GITT) curves of (a) PNVO-1 and (b) PNVO-3 at 1A. (c) Zoomed-in voltage-time curves for PNVO-2.

GITT was employed to evaluate the Zn^{2+} diffusion dynamics for VO, PVO, PNVO-1, PNVO-2 and PNVO-3 electrodes. The value of diffusion coefficients for the electrode can be further quantified by employing the following equation:[3]

$$D_{Zn^{2+}} = \frac{4}{\pi\tau}\left(\frac{m_B V_M}{M_B S}\right)\left(\frac{\Delta E_s}{\Delta E_\tau}\right)^2 \quad \text{(S1)}$$

Where m_B is the mass of the active materials in the electrode, M_B and V_M are the molar mass and molar volume of the electrode material, respectively, and S is the surface area of the electrode.

Figure S19 shows the GITT curves of PNVO-1 (a) and PNVO-3 (b) at 1 A g^{-1}, and the relaxation time was set to 30 min with a pulse time of 1 min (c). The ion diffusion coefficient of PNVO-1 and PNVO-3 during the charge and discharge was calculated ranging 10^{-11} cm² s^{-1} to 10^{-9} cm² s^{-1}.

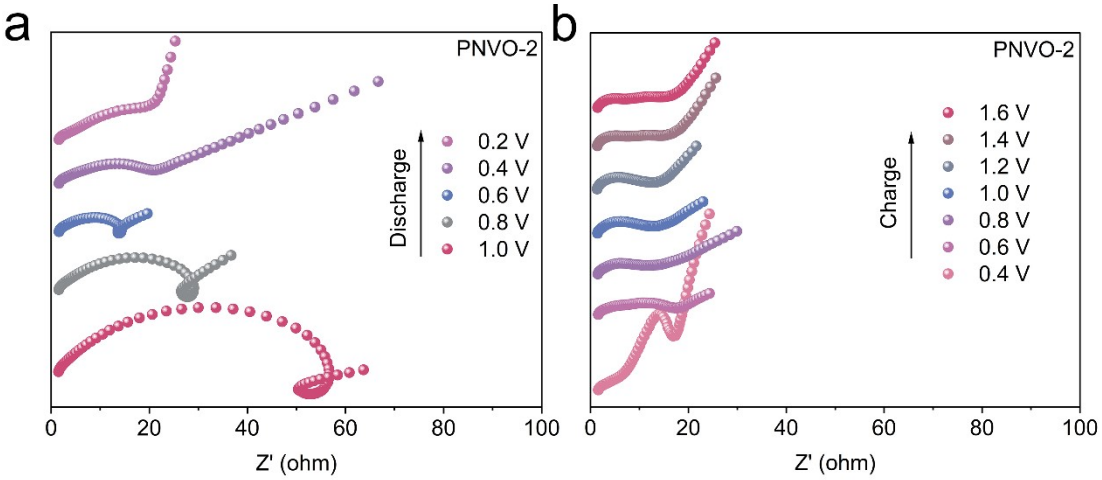

Figure S20. Nyquist plots of the PNVO-2 at different (a) discharge and (b) charge states.

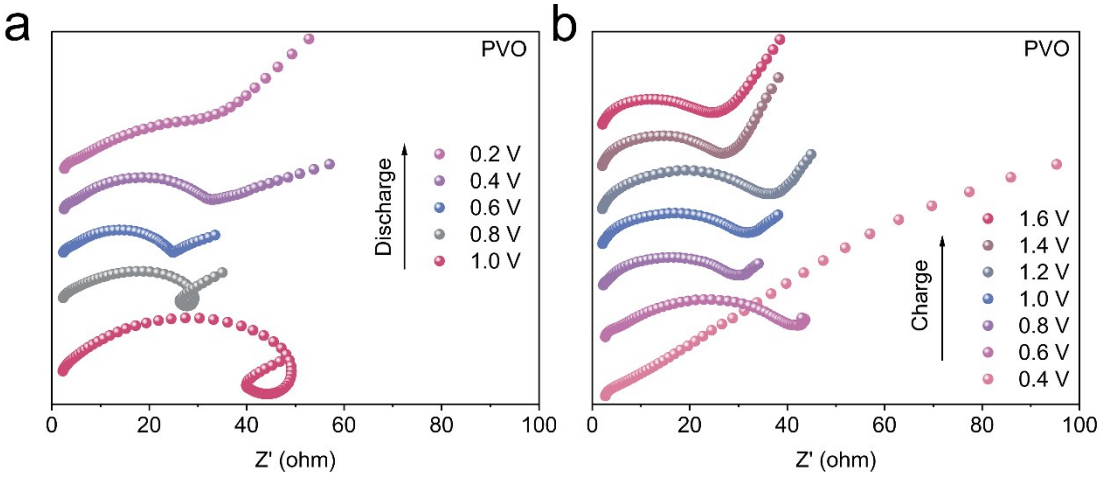

Figure S21. Nyquist plots of the PVO at different (a) discharge and (b) charge states.

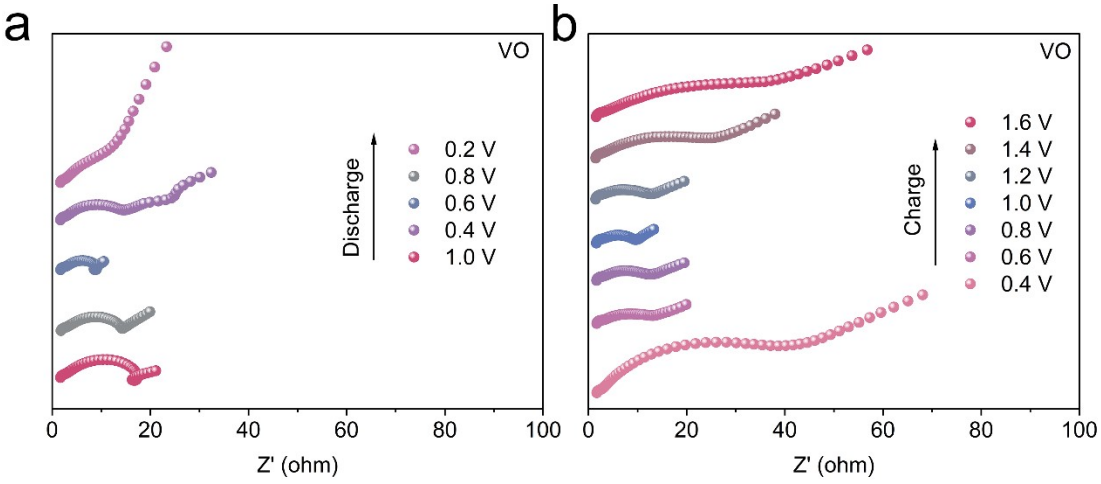

Figure S22. Nyquist plots of the VO at different (a) discharge and (b) charge states.

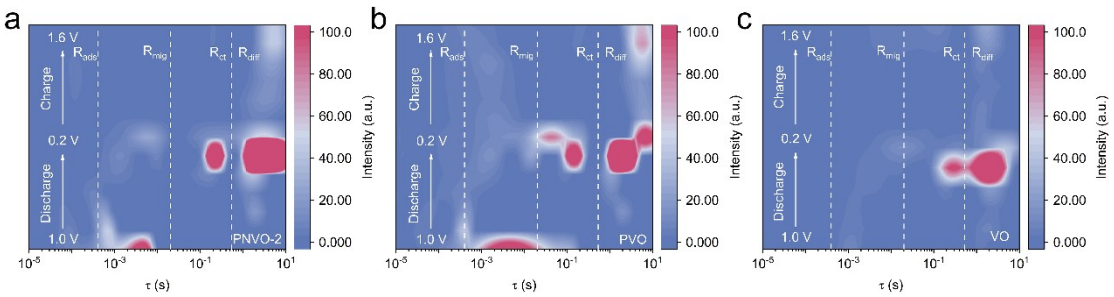

Figure S23. 2D intensity maps of the distribution of relaxation times (DRT) for (a) PNVO-2, (b) PVO and (c) VO.

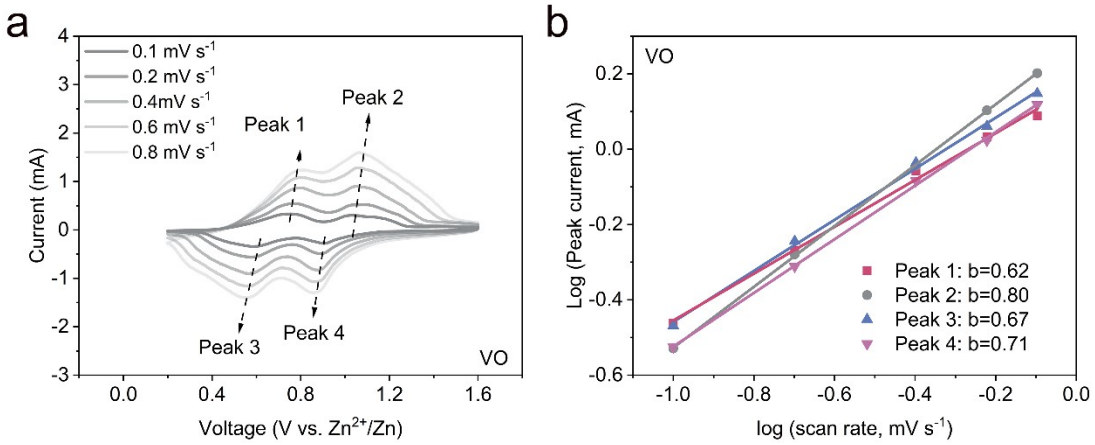

Figure S24. (a) CV curves for VO at various scan rates and (b) the corresponding plots of log (i) versus log (v) plots.

The peak current (i) in the CV curves with scan rate (υ) obeys the law as follows:[4]

$$i = a\upsilon^{b} \quad \text{(S2)}$$

$$\log(i)=b\log(\upsilon)+\log(a) \quad \text{(S3)}$$

where a and b are variables. The b value can be determined from the slope of the log(i) vs. log(υ). The b-value of 0.5 demonstrates that the electrochemical behavior is mainly diffusion controlled, while the b-value of 1.0 means that the electrochemical behavior is capacitive-controlled.[5] And the calculated results of b value suggest their electrochemical behaviors are controlled by diffusion and capacitance. To further quantify the pseudocapacitive contribution, the current response can be divided into two separated processes:[6]

$$i(\upsilon) = k_1\upsilon + k_2\upsilon^{1/2} \quad \text{(S4)}$$

$$i(\upsilon)/\upsilon^{1/2} = k_1\upsilon^{1/2} + k_2 \quad \text{(S5)}$$

where $k_1\upsilon$ and $k_2\upsilon^{1/2}$ correspond to the current contributions from the capacitive-controlled and the diffusion-controlled process, respectively.

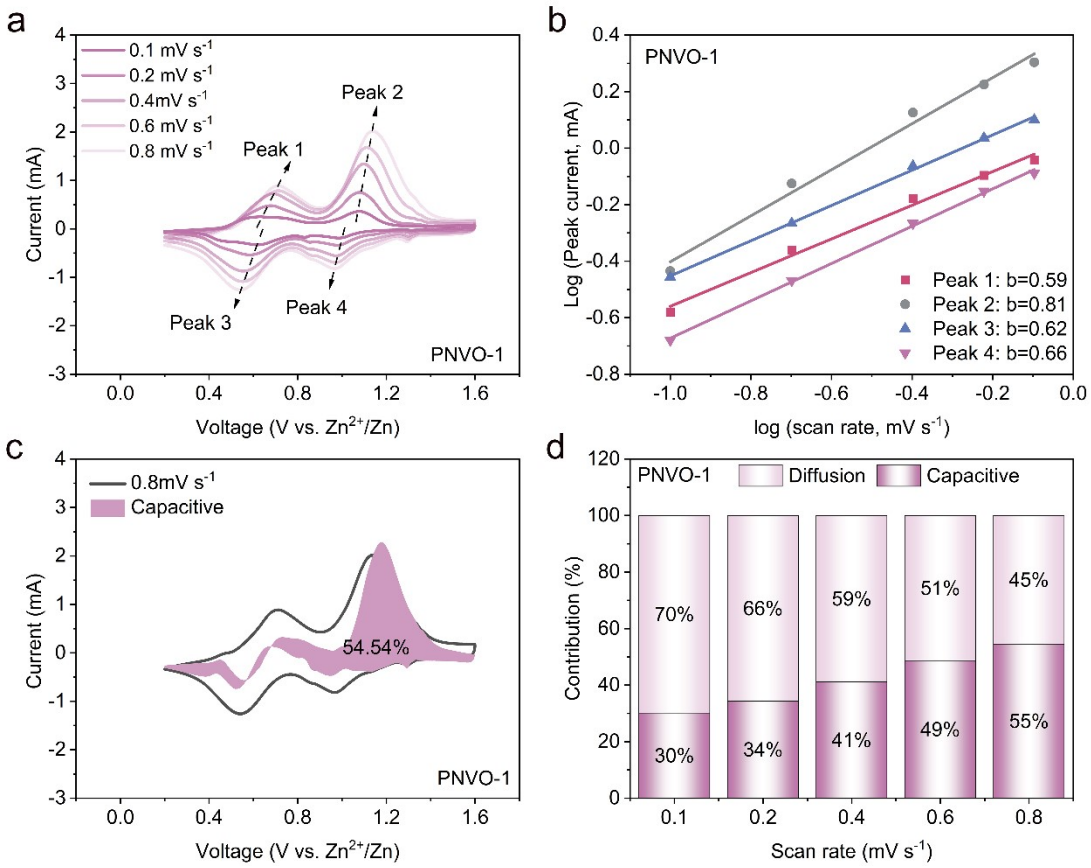

Figure S25. (a) CV curves for PNVO-1 at various scan rates and (b) the corresponding plots of log (i) versus log (v) plots. (c) pseudocapacitive contribution for PNVO-1 at 0.8 mVs^{-1}. (d) Capacity contribution ratios at various scan rates.

Figure S25a displays the CV curves of PNVO-1 at different scan rates ranging from 0.1 to 0.8 mV s^{-1}. The intensities of the redox peaks were intensified with the increase of scan rate.[7] The correlation between the peak current and scan rate was fitted in Figure S25b, and the calculated b values were 0.59, 0.81, 0.62 and 0.66, suggesting the electrochemical process was collaboratively controlled by diffusion and capacitive behaviors. Figure S25c illustrates the capacitive contribution of PNVO-1 at 0.8 mV s^{-1}, and the contribution ratio was calculated to 54%. Figure S25d exhibits the capacitive contribution ratios of PNVO-1 at different scan rates. The ratios of PNVO-1 were 54%, 59%, 67%, 75% and 76% at 0.1 mV s^{-1}, 0.2 mV s^{-1}, 0.4 mV s^{-1} and 0.8 mV s^{-1}.

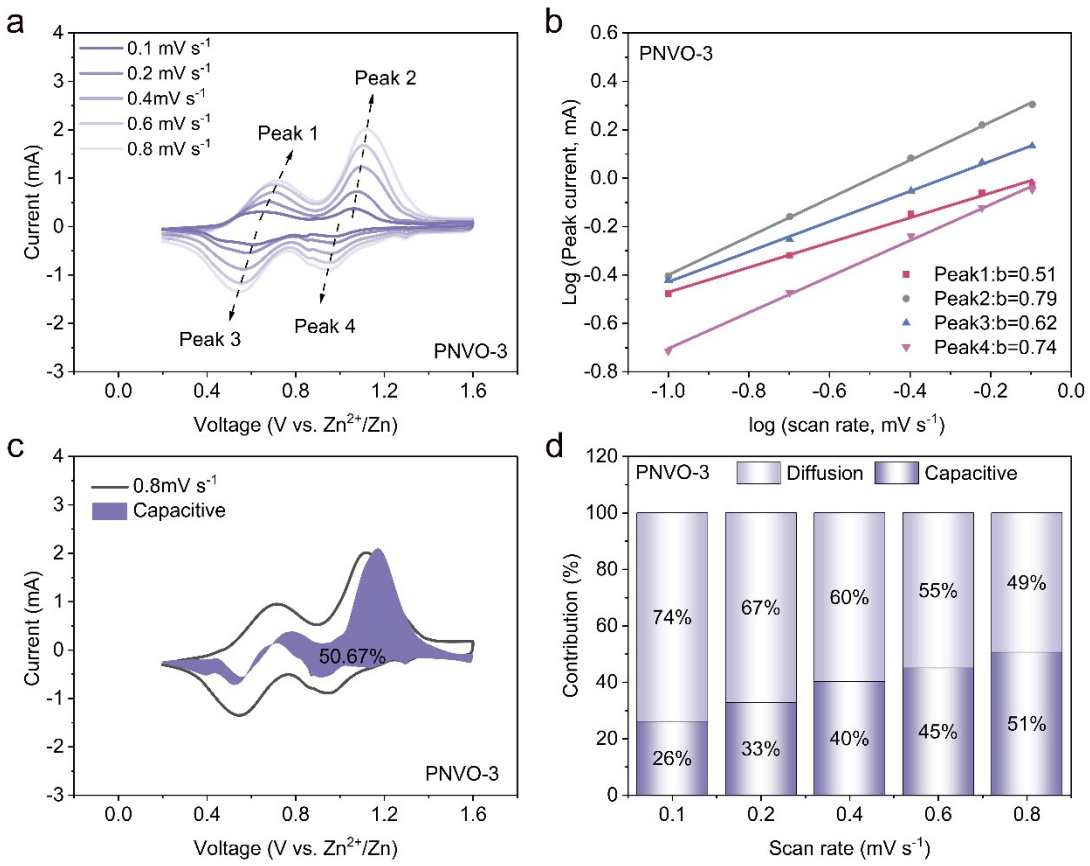

Figure S26. (a) CV curves for PNVO-3 at various scan rates and (b) the corresponding plots of log (i) versus log (v) plots. (c) pseudocapacitive contribution for PNVO-3 at 0.8 mVs^{-1}. (d) Capacity contribution ratios at various scan rates.

Figure S26a displays the CV curves of PNVO-3 at different scan rates ranging from 0.1 to 0.8 mV s^{-1}. The intensities of the redox peaks were intensified with the increase of scan rate. The correlation between the peak current and scan rate was fitted in Figure S26b, and the calculated b values were 0.51, 0.79, 0.62 and 0.74, suggesting the electrochemical process was collaboratively controlled by diffusion and capacitive behaviors. Figure S26c illustrates the capacitive contribution of PNVO-3 at 0.8 mV s^{-1}, and the contribution ratio was calculated to 50%. Figure S26d exhibits the capacitive contribution ratios of PNVO-3 at different scan rates. The ratios of PNVO-1 were 30%, 34%, 41%, 49% and 55% at 0.1 mV s^{-1}, 0.2 mV s^{-1}, 0.4 mV s^{-1} and 0.8 mV s^{-1}.

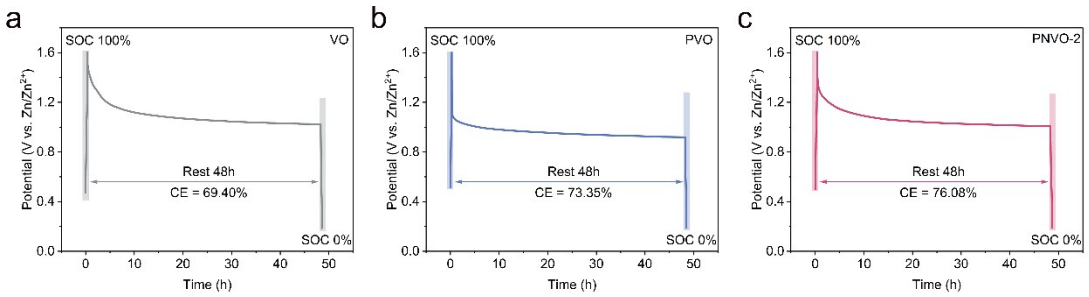

Figure S27. Self-discharge tests of Zn // VO, Zn // PVO and Zn // PNVO-2 cells.

Self-discharge tests were conducted on the full-cell to investigate the charge retention capability and stability of the electrode materials.[8] After a 48h resting, the PNVO-2 cathode exhibited a high Coulombic efficiency of 76.08%, surpassing the 69.40% and 73.35% of VO and PVO, respectively. This indicates the superior structural stability of PNVO-2. Such stability can be attributed to the pillar effect of Nb^{5+} intercalation, which reinforces the structural integrity.

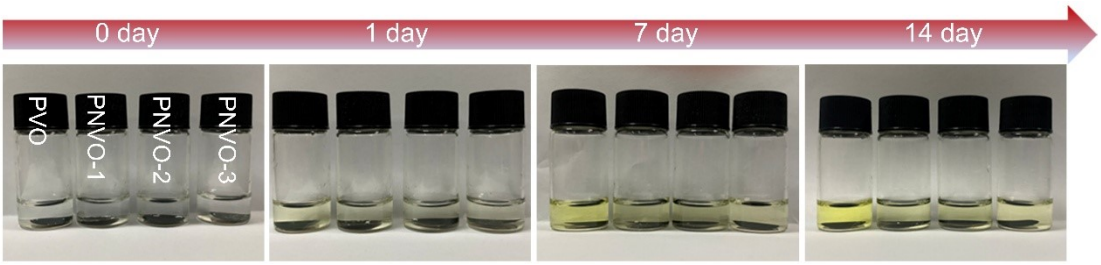

Figure S28. Photos of PVO, PNVO-1, PNVO-2 and PNVO-3 soaked in 2M $ZnSO_4$ electrolyte for different time.

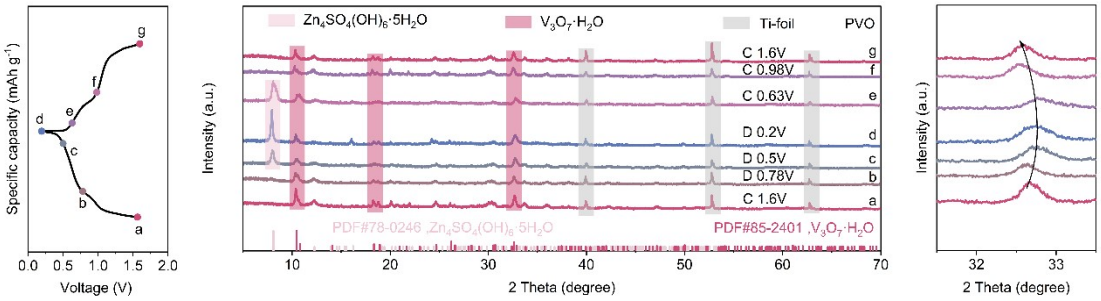

Figure S29. Ex-situ XRD patterns of PVO at 2 A g^{-1}.

Figure S29 shows the ex situ XRD patterns of PVO. During the discharge process, the diffraction peak at ~32° was gradually shifted toward high degree, indicating a decrease in interlayer spacing that was attributed to the strong electrostatic attraction between the V_3O_7 interlayers and the inserted Zn^{2+} ions.[9] And the peak was then shifted to the origin position after charge, indicating good reversibility. Meanwhile, A new diffraction peak emerges at ~ 7.9° when discharging to 0.5 V, corresponding to the by-product $Zn_4SO_4(OH)_6·5H_2O$ (PDF#78-0246), and this peak begins to disappear upon charging above 0.63 V.

References

1 X. Bi, A. Yu, J. Zhang, J. Yu, C. Li, Y. Ren, K. Lin, J. Chai, Q. Xue, Y. Xie, Y. Cheng, X. Chang, X. Lu, L. Yang, R. He, G. Zeng, C. Huang, X. Qi, X. Qi, C. Zhang, J. Arbiol, T. Jacob and A. Cabot, Ca^{2+}-Preintercalated V_2O_5 as a Dual-Function Cathode Additive for Polyiodide Anchoring in Zn–I_2 Batteries, *ACS Nano*, 2025, **19**, 25438–25454.

2 Q. Zhu, Z. Wang, J. Wang, X. Liu, dan Yang, L. Cheng, M. Tang, Y. Qin and H. Wang, Challenges and strategies for ultrafast aqueous zinc-ion batteries, *Rare Met.*, 2021, **40**, 309–328.

3 Q. Li, C. Wang, Y. Zhu, W. Du, W. Liu, M. Yao, Y. Wang, Y. Qian and S. Feng, Unlocking the critical role of Mg doping in α-MnO_2 cathode for aqueous zinc ion batteries, *Chemical Engineering Journal*, 2024, **485**, 150077.

4 F. Zhang, M. Du, Z. Miao, H. Li, W. Dong, Y. Sang, H. Jiang, W. Li, H. Liu and S. Wang, Oxygen vacancies and N-doping in organic–inorganic pre-intercalated vanadium oxide for high-performance aqueous zinc-ion batteries, *InfoMat*, 2022, **4**, e12346.

5 Y. Zhang, Q. Li, W. Feng, S. Gao, H. Yue, Y. Su, H. Zhou, J. Huang, L. Han, M. Shakouri, Y. Wang and H. Pang, Regulating Electron Transfer in Vanadium-Based Metal–Organic Frameworks via the Synergy of Linker Engineering and Machine Learning for Efficient and Reversible Aqueous Zinc Ion Batteries, *Advanced Materials*, 2025, **37**, 2507609.

6 L. Xing, C. Zhang, M. Li, P. Hu, X. Zhang, Y. Dai, X. Pan, W. Sun, S. Li, J. Xue,

Q. An and L. Mai, Revealing excess Al3+ preinsertion on altering diffusion paths of aluminum vanadate for zinc-ion batteries, *Energy Storage Materials*, 2022, **52**, 291–298.

7 C. Zhang, Y. Huang, X. Xu, Z. Chen, G. Xiao, Y. Zhong, X. Wang, C. Gu and J. Tu, Bulk-to-surface co-modification of layered hydrated vanadate cathode for aqueous zinc ion batteries, *Energy Environ. Sci.*, 2024, **17**, 4090–4103.

8 B. Fan, C. Huang, Z. Jiang, K. Song, B. Xu, A. Wei, W. Zhang and W. Zheng, Decoupling Electronic and Crystal Structure Effects to Overcome the Capacity-Stability Trade-Off for High-Performance Aqueous Zinc-Ion Batteries, *Adv Funct Materials*, 2025, e22400.

9 H. Tang, K. Wan, K. Zhang, A. Wang, M. Wang, J. Xie, P. Su, H. Dong, J. Sun and Y. Li, Realizing Dual-Mode Zinc-Ion Storage of Generic Vanadium-Based Cathodes via Organic Molecule Intercalation, *ACS Nano*, 2024, **18**, 30896–30909.